Transient Thermal Modeling of a Power Module: An N-Layer Fourier Approach

Khaled Redwan Choudhury and Daniel J. Rogers, *Senior Member, IEEE*

***Abstract*—A transient model of a rectangular N-layer structure with an arbitrary number of rectangular heat sources on the top surface is obtained by Fourier series solution. As power modules can be closely approximated by this type of structure, the model may be used to accurately estimate the temperature field occurring in such modules. The Fourier-based method developed in this work is compared with a finite-element model and an excellent matching (under 2% error) in the transient region is found. An experimental validation is performed using a half-bridge silicon carbide power module monitored by a high frame-rate thermal camera. After the model outputs have been compensated to match the limited frequency response of the camera, a good matching is found between model and experiment (under 6% error).**

***Index Terms*—Experiment, Fourier series, power module, simulation, transient thermal modeling, verification.**

NOMENCLATURE

i	Layer no. [1, 2,.., N].
$\bar{m}$	Index of the summation in the Fourier expansion in the x-direction [1, 2,..].
$\bar{n}$	Index of the summation in the Fourier expansion in the y-direction [1, 2,..].
a, b, c, d	Linear dimensions (m).
Q	Step input power dissipation (W).
A_{i0}, B_{i0}	Zeroth-order Fourier coefficients temperature variation in the y-direction for a constant z.
$A_{\bar{m}\bar{n}\bar{l}}$	Fourier coefficients in transient solution.
θ_i	Temperature-rise of in the ith layer w.r.t the temperature of the fluid or the isothermal surface.
k_i	Thermal conductivity of the ith layer (W/(mK)).
ρ_i	Density of the ith layer (kg/m^3).
c_i	Specific heat capacity of the ith layer (J/(KgK)).
α_i	Thermal diffusivity of the ith layer (m^2/s).

I. INTRODUCTION

SILICON and silicon carbide-based power modules are common in power electronic systems because of their high heat transfer capability, high power density, and improved reliability when compared to discrete component solutions. The use of power modules in automotive, rail-traction, and motor-drive applications is well established. In these applications, the environmental and load-imposed thermal cycling or the combination of both can result in not only high peak junction temperature [1]–[3], but also large, frequent, and unpredictable fluctuations in junction temperature [4]. For example, in wind turbine systems, the mission profile is stochastic due to the variation of wind speed [5]. It is known that large fluctuations in the junction temperature can result in the failure of solder layers and the breaking of bond wires due to the mismatch in coefficients of the thermal expansion of different materials [6]. In this context, accurate modeling of the temperature profile (both in time and space) of the semiconductor dies becomes important.

The accurate estimation of the time-varying junction temperature is of interest in the real-time control, health management, and active thermal management of power electronic converters [7], [8]. Methods to estimate the junction temperature profile are demonstrated in [9] and [10] for the implementation of real-time health management in applications with an uncertain load-profile. Additionally, it is often suggested that a continuous monitoring of junction temperature as a failure indicator is required to enable effective prognostics of semiconductor devices [11], [12]

From the above discussion, it is clear that not only the steady-state value of the junction temperature but also the transient response of the semiconductor devices to varying heat loads is important when trying to predict or monitor system lifetime. Therefore, transient thermal modeling is an important addition to steady-state thermal modeling. Steady-state thermal modeling of power modules has been investigated in a number of ways. For example, the finite-element method and finite-difference method have been used in [13] and [14], respectively, although mesh-based methods can require long computational time, which may restrict them to nonreal-time applications [15]. Compact or reduced order electro-thermal models [16]–[20] based on *RC* networks may be fast and accurate enough for real-time applications. However, it is difficult to take into account thermal cross-coupling effects in these models and these models are generally defined under a specific boundary condition of a constant ambient temperature [21]. In [22] and [23], compact thermal models for the early-stage design of integrated circuits are proposed where the stack of different layers of electronic packaging is divided into a number of nodes to form a grid. These nodes are connected to each other by *RC* elements. In essence, these models use a finite-element/finite-difference

---

Manuscript received September 24, 2019; revised February 4, 2020; accepted March 13, 2020. Date of publication March 30, 2020; date of current version June 23, 2020. Recommended for publication by Associate Editor K. Ngo. *(Corresponding author: Khaled Redwan Choudhury.)*

The authors are with the Power Electronics Group University of Oxford, Oxford OX1 2JD, U.K. (e-mail: khaled.choudhury@wolfson.ox.ac.uk; dan.rogers@eng.ox.ac.uk).

Color versions of one or more of the figures in this article are available online at https://ieeexplore.ieee.org.

Digital Object Identifier 10.1109/TPEL.2020.2983248

approach targeted at specific applications. It is worth noting that relevant, similar heat transfer problems, and solution methods can be found in some disciplines other than electrical/electronic engineering. For example, in [24], a two-dimensional (2-D) transient thermal modeling of a floor-space heating system is developed. This work was extended to the 3-D case in [25]. In [26], an exact solution of 2-D heat conduction in a two-layered body of composite materials is developed which was applied in aerospace applications. Transient thermal characteristics of two-layered body with isotropic materials have been studied in [27]. In a similar way, Fourier series-based analytical or semianalytical solutions developed in other disciplines may be used for the thermal modeling in microelectronics and integrated circuits. For example, an analysis of the thermal response of power chip packages is presented in [28]. This article is theoretically important but it deals with only one-layer structures. An analytical and spectral domain decomposition approach is adopted in [29]. This method is robust and can take into account the nonlinearity of thermal conductivities in the system, but it is difficult to implement because of the complicated inverse Laplace transform associated with it. In [30], a semianalytical approach based on Green's function is used to determine the steady-state and transient temperature field in 3-D integrated circuits, although the rationale behind using a particular form of auxiliary function for thermal modeling is not very clear. In [31], a thermal simulation tool for integrated circuits, microsystem, and multichip modules is presented based on the fast Fourier transformation (FFT); hence, it is relatively complex to implement. Again, in [32] a 3-D thermal model for hybrid or monolithic integrated power circuits is developed with the use of the FFT. Although useful, these solutions have not found much application in power electronics, possibly because of the apparent complexity of the implementation. Recently, we presented a Fourier series-based approach for the the steady-state thermal modeling of power modules [33]. We now extend that approach to tackle the transient thermal modeling of power module. Here, the transient thermal model of a rectangular structure with an arbitrary number of layers containing an arbitrary number of rectangular heat sources on its topmost surface is presented. This model is accurate and relatively straightforward to implement. It is then applied to the power module. The model is verified using the finite-element modeling (FEM) package COMSOL Multiphysics and by experiment. The major advantage of the method presented in this article over mesh methods, such as FEM, is that it can evaluate the temperature of a single point quickly, in contrast to mesh methods where the entire temperature field must be found. This potentially makes the method suitable for real-time applications. In addition, Fourier-based methods are smooth with dimensional changes and hence the method may be readily applied to the numerical optimisation of power module designs using standard optimization frameworks.

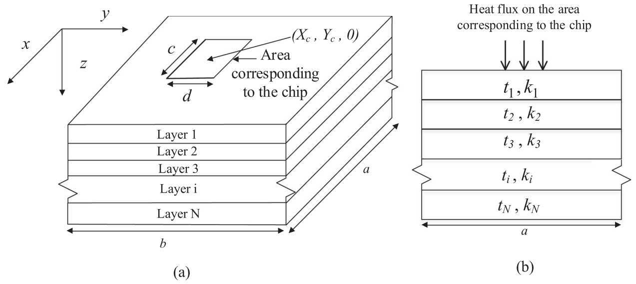

(a) (b)

Fig. 1. (a) N-layer structure. (b) Side view of the structure with heat flux.

II. Problem Statement

The physical structure is identical to that used in [33] and is repeated here for clarity. Let us consider a rectangular structure with N different layers containing only one rectangular heat source, as shown in Fig. 1 (the effect of multiple heat sources will be considered later). The rectangular heat source is situated on the surface of layer 1. The position of the source is given by its centre $(X_C, Y_C, 0)$ and its length and width are c and d, respectively. This source generates heat Q uniformly over the surface it is situated. It is also assumed all the surfaces of the rectangular structure are adiabatic (insulated) except the bottom surface which is subject to convective heat transfer. The system is governed by the following:

$$\frac{\partial^2 \theta_i}{\partial x^2} + \frac{\partial^2 \theta_i}{\partial y^2} + \frac{\partial^2 \theta_i}{\partial z^2} = \frac{1}{\alpha_i} \frac{\partial \theta_i}{\partial t}. \tag{1}$$

At $t = 0$, the initial condition is

$$\theta_i = 0. \tag{2}$$

The heat flux is a step input such that it changes instantaneously from zero for $t < 0$ to q_0 for $t \geq 0$. θ_i can be written as a sum of the steady-state solution ($\theta_{i,s}$) and the transient solution ($\theta_{i,t}$)

$$\theta_i = \theta_{i,s} + \theta_{i,t}. \tag{3}$$

Now, $\theta_{i,s}$ is subject to the following boundary conditions. For the first layer and underneath the heat source

$$\left. \frac{\partial \theta_{1,s}}{\partial z} \right|_{z=0} = -\frac{q_0}{k_1} = -\frac{Q}{k_1\, cd}. \tag{4}$$

Outside the source, the boundary condition is

$$\left. \frac{\partial \theta_{1,s}}{\partial z} \right|_{z=0} = 0. \tag{5}$$

Because of the adiabatic sides of the structure

$$\left. \frac{\partial \theta_{i,s}}{\partial x} \right|_{x=0,a} = 0 \text{ and } \left. \frac{\partial \theta_{i,s}}{\partial y} \right|_{y=0,b} = 0.$$

Assuming perfect thermal contact between the layers, the boundary conditions at the interfaces are

$$k_i \left. \frac{\partial \theta_{i,s}}{\partial z} \right|_{z=z_i} = k_{i+1} \left. \frac{\partial \theta_{(i+1),s}}{\partial z} \right|_{z=z_i} \tag{6}$$

and

$$\theta_{i,s}(x, y, z_i) = \theta_{(i+1),s}(x, y, z_i) \tag{7}$$

where

$$z_i = \sum_{j=1}^{i} t_j.$$

The boundary condition for the bottom layer is

$$k_N \left.\frac{\partial \theta_{N,s}}{\partial z}\right|_{z=z_N} = -h\theta_{N,s} \tag{8}$$

where h is the coefficient of convective heat transfer which couples the system to the ambient temperature.

$\theta_{i,t}$ is subject to similar boundary conditions for $t \geq 0$ except

$$\left.\frac{\partial \theta_{1,t}}{\partial z}\right|_{z=0} = 0 \tag{9}$$

and

$$\left.\theta_{N,t}\right|_{z=z_N} = 0. \tag{10}$$

III. PROBLEM SOLUTION: TRANSIENT RECTANGULAR N-LAYER FOURIER (TRNLF) METHOD

The steady-state part of (3) is derived in [33]. For the transient part, the governing equation and all the boundary conditions are linear and homogeneous. Therefore, the transient problem can be solved by the separation of variables method [34]. The transient solution can be expressed as

$$\theta_{i,t} = \sum_{\bar{m}=0}^{\infty}\sum_{\bar{n}=0}^{\infty}\sum_{\bar{l}=1}^{\infty} A_{\bar{m}\bar{n}\bar{l}} X_{i\bar{m}}(x) Y_{i\bar{n}}(y) Z_{i\bar{l}}(z) T_i(t). \tag{11}$$

As we are mainly interested in the temperature distribution of the first layer, it is sufficient to know $\theta_{1,t}$ which is given by

$$\theta_{1,t} = \sum_{\bar{m}=0}^{\infty}\sum_{\bar{n}=0}^{\infty}\sum_{\bar{l}=1}^{\infty} A_{\bar{m}\bar{n}\bar{l}} X_{1\bar{m}}(x) Y_{1\bar{n}}(y) Z_{1\bar{l}}(z) \exp(-\zeta^2 t) \tag{12}$$

where

$$X_{1\bar{m}}(x) = \cos\left(\frac{\bar{m}\pi}{a}x\right), Y_{1\bar{n}}(y) = \cos\left(\frac{\bar{n}\pi}{b}y\right)$$

and

$$Z_{1\bar{l}}(z) = A_{1\bar{l}} \sin\left(\frac{\nu_{\bar{l}} z}{\sqrt{\alpha_1}}\right) + B_{1\bar{l}} \cos\left(\frac{\nu_{\bar{l}} z}{\sqrt{\alpha_1}}\right)$$

and

$$T_1(t) = \exp(-\zeta^2 t).$$

Here

$$\zeta^2 = \left(\frac{\bar{m}\pi\sqrt{\alpha_1}}{a}\right)^2 + \left(\frac{\bar{n}\pi\sqrt{\alpha_1}}{b}\right)^2 + \nu_{\bar{l}}^2.$$

The complete procedure to determine temperature of a particular point in space and time is described in Fig. 2. The first step of the solution is to form the relevant matrix from which the eigenvalues will be determined. After that, coefficients in $Z_{i\bar{l}}$ are determined corresponding to each eigenvalue. These are subsequently used for the determination of temperature. The relevant coefficients and eigenvalues ($\nu_{\bar{l}}$) are calculated in the next sections.

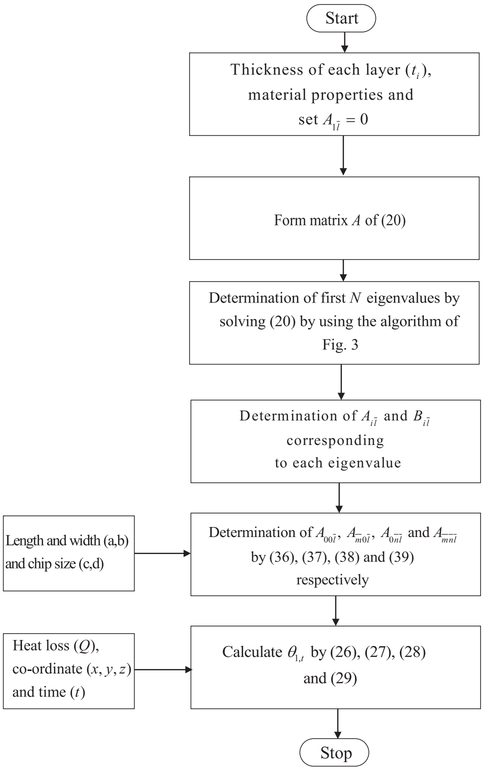

Fig. 2. Flowchart to determine the temperature at a point in time and space.

A. Generalized Orthogonal Expansion Technique

This technique is well documented in [34] for 1-D cases. It can be extended for 3-D cases as follows.

1) Determination of the Eigenvalues: For the sake of clarity, a rectangular structure of two layers is considered here. The eigenfunctions corresponding to each layer are given as follows:

$$Z_{1\bar{l}}(z) = A_{1\bar{l}} \sin\left(\frac{\nu_{\bar{l}} z}{\sqrt{\alpha_1}}\right) + B_{1\bar{l}} \cos\left(\frac{\nu_{\bar{l}} z}{\sqrt{\alpha_1}}\right) \tag{13}$$

$$Z_{2\bar{l}}(z) = A_{2\bar{l}} \sin\left(\frac{\nu_{\bar{l}} z}{\sqrt{\alpha_2}}\right) + B_{2\bar{l}} \cos\left(\frac{\nu_{\bar{l}} z}{\sqrt{\alpha_2}}\right). \tag{14}$$

Applying (9) to (13), $A_{1\bar{l}}$ is found to be 0. Therefore

$$Z_{1\bar{l}}(z) = B_{1\,l'} \cos\left(\frac{\nu_{l'} z}{\sqrt{\alpha_1}}\right). \tag{15}$$

Now, applying relevant boundary conditions to (13) and (14); it is found that

$$\frac{k_1}{k_2}\frac{B_{1\bar{l}}}{\sqrt{\alpha_1}} \sin\left(\frac{\nu_{\bar{l}} t_1}{\sqrt{\alpha_1}}\right) + \frac{A_{2\bar{l}}}{\sqrt{\alpha_2}} \cos\left(\frac{\nu_{\bar{l}} t_1}{\sqrt{\alpha_2}}\right) - \frac{B_{2\bar{l}}}{\sqrt{\alpha_2}} \sin\left(\frac{\nu_{\bar{l}} t_1}{\sqrt{\alpha_2}}\right) = 0 \tag{16}$$

$$B_{1\bar{l}} \cos\left(\frac{\nu_{\bar{l}} t_1}{\sqrt{\alpha_1}}\right) - A_{2\bar{l}} \sin\left(\frac{\nu_{\bar{l}} t_1}{\sqrt{\alpha_2}}\right) - B_{2\bar{l}} \cos\left(\frac{\nu_{\bar{l}} t_1}{\sqrt{\alpha_2}}\right) = 0 \tag{17}$$

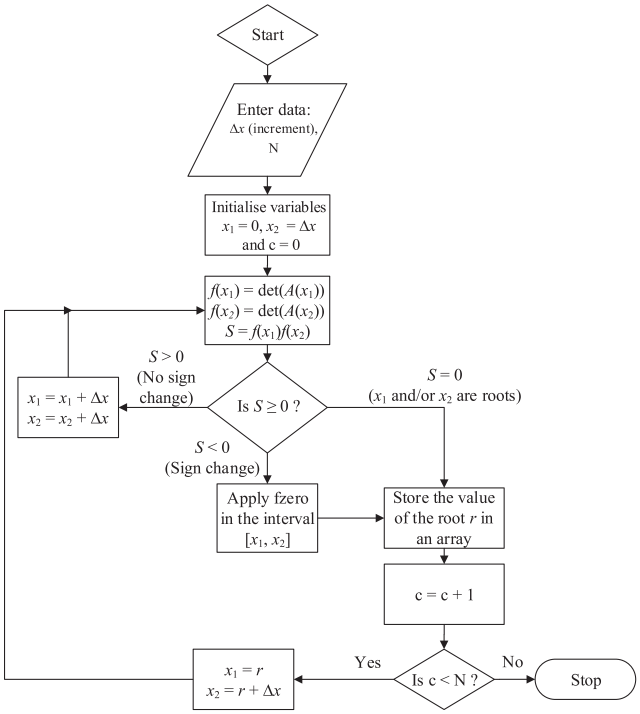

Fig. 3. Flowchart to determine the first N eigenvalues.

and

$$A_{2\bar{l}}\sin\left(\frac{\nu_{\bar{l}}(t_1+t_2)}{\sqrt{\alpha_2}}\right)+B_{2\bar{l}}\cos\left(\frac{\nu_{\bar{l}}(t_1+t_2)}{\sqrt{\alpha_2}}\right)=0. \quad (18)$$

Therefore

$$AX=0 \quad (19)$$

where A is given by the following matrix:

$$\begin{bmatrix} \frac{k_1}{k_2}\frac{1}{\sqrt{\alpha_1}}\sin\left(\frac{\nu_{\bar{l}}t_1}{\sqrt{\alpha_1}}\right) & \frac{1}{\sqrt{\alpha_2}}\cos\left(\frac{\nu_{\bar{l}}t_1}{\sqrt{\alpha_2}}\right) & -\frac{1}{\sqrt{\alpha_2}}\sin\left(\frac{\nu_{\bar{l}}t_1}{\sqrt{\alpha_2}}\right) \\ \cos\left(\frac{\nu_{\bar{l}}t_1}{\sqrt{\alpha_1}}\right) & -\sin\left(\frac{\nu_{\bar{l}}t_1}{\sqrt{\alpha_2}}\right) & -\cos\left(\frac{\nu_{\bar{l}}t_1}{\sqrt{\alpha_2}}\right) \\ 0 & \sin\left(\frac{\nu_{\bar{l}}(t_1+t_2)}{\sqrt{\alpha_2}}\right) & \cos\left(\frac{\nu_{\bar{l}}(t_1+t_2)}{\sqrt{\alpha_2}}\right) \end{bmatrix}$$

and

$$X=\begin{bmatrix} B_{1\bar{l}} \\ A_{2\bar{l}} \\ B_{2\bar{l}} \end{bmatrix}.$$

Now, For X to have a nontrivial solution the following relation must hold:

$$\det(A)=0. \quad (20)$$

This is a transcendental equation and it must be solved numerically to find the first N eigenvalues $(\nu_1,\nu_2,\nu_3,\nu_4,\ldots,\nu_N)$. The algorithm used in this work is described in Fig. 3. The basic idea of this algorithm is to sample det(A) at a regular interval Δx starting from 0 to find a sign-change of that function. If a sign-change occurs, a built-in MATLAB function fzero is used to find a root related to that sign-change. This process continues until N eigenvalues are found.

2) Determination of the Coefficients of the Eigenfunctions: The system described by (20) is linear and homogeneous. Therefore, the nontrivial solution of (20) can be expressed as a multiple of any Fourier coefficients. Therefore, without the loss of generality $B_{1\bar{l}}$ can be considered equal to 1. Setting $B_{1\bar{l}}=1$ in (16) and (17), a set of Fourier coefficients can be obtained corresponding to each eigenvalue by using any standard method (for example, matrix inversion or Cramer's rule). For example, A_{21} and B_{21} can be obtained from ν_1, A_{22} and B_{22} can be obtained from ν_2 and so on. It is important to highlight that matrix A is independent of a and b or the position of the chip. Therefore, determination of eigenvalues and relevant coefficients depends only on the material properties and thickness of each layer.

B. Determination of $A_{00\bar{l}}$, $A_{\bar{m}0\bar{l}}$, $A_{0\bar{n}\bar{l}}$, and $A_{\bar{m}\bar{n}\bar{l}}$

Now, it remains to find $A_{\bar{m}\bar{n}\bar{l}}$ [of (12)] which can be expressed by the following equation:

$$A_{\bar{m}\bar{n}\bar{l}}=\frac{1}{N_{\bar{m}}N_{\bar{n}}N_{\bar{l}}}(S_1+S_2) \quad (21)$$

where

$$S_1=\frac{k_1}{\alpha_1}\int_0^a\int_0^b\int_0^{t_1}\left(F_1(x,y,z)\cos\left(\frac{\bar{m}\pi}{a}x\right)\times\cos\left(\frac{\bar{n}\pi}{b}y\right)Z_{1\bar{l}}\right)\mathrm{d}x\mathrm{d}y\mathrm{d}z$$

and

$$S_2=\frac{k_2}{\alpha_2}\int_0^a\int_0^b\int_{t_1}^{t_1+t_2}\left(F_2(x,y,z)\cos\left(\frac{\bar{m}\pi}{a}x\right)\times\cos\left(\frac{\bar{n}\pi}{b}y\right)Z_{2\bar{l}}\right)\mathrm{d}x\mathrm{d}y\mathrm{d}z.$$

Here, F_1 and F_2 are initial temperature distributions in layer 1 and 2, respectively. $N_{\bar{m}}$, $N_{\bar{n}}$, and $N_{\bar{l}}$ are given by the following equations:

$$N_{\bar{m}}=\int_0^a\cos^2\left(\frac{\bar{m}\pi}{a}x\right)\mathrm{d}x=\begin{cases} a & \text{if } \bar{m}=0 \\ a/2 & \text{otherwise}\end{cases} \quad (22)$$

$$N_{\bar{n}}=\int_0^b\cos^2\left(\frac{\bar{n}\pi}{b}y\right)\mathrm{d}y=\begin{cases} b & \text{if } \bar{n}=0 \\ b/2 & \text{otherwise}\end{cases} \quad (23)$$

$$N_{\bar{l}}=\frac{k_1}{\alpha_1}\int_0^{t_1}Z_{1\bar{l}}^2\mathrm{d}z+\frac{k_2}{\alpha_2}\int_{t_1}^{t_1+t_2}Z_{2\bar{l}}^2\mathrm{d}z. \quad (24)$$

Now, for ease of implementation (12) can be written as

$$\theta_{1,t}=M_1+M_2+M_3+M_4 \quad (25)$$

where

$$M_1=\sum_{\bar{l}=1}^{\infty}A_{00\bar{l}}Z_{1\bar{l}}\exp(-t\nu_{\bar{l}}^2) \quad (26)$$

$$M_2 = \sum_{\bar{m}=1}^{\infty}\sum_{\bar{l}=1}^{\infty}\left(A_{\bar{m}0\bar{l}}\cos\left(\frac{\bar{m}\pi}{a}x\right)Z_{1\bar{l}}\right.$$
$$\left.\exp\left(-t\left(\left(\frac{\bar{m}\pi\sqrt{\alpha_1}}{a}\right)^2+\nu_{\bar{l}}^2\right)\right)\right) \tag{27}$$

$$M_3 = \sum_{\bar{n}=1}^{\infty}\sum_{\bar{l}=1}^{\infty}\left(A_{0\bar{n}\bar{l}}\cos\left(\frac{\bar{n}\pi}{b}y\right)Z_{1\bar{l}}\right.$$
$$\left.\exp\left(-t\left(\left(\frac{\bar{n}\pi\sqrt{\alpha_1}}{b}\right)^2+\nu_{\bar{l}}^2\right)\right)\right) \tag{28}$$

$$M_4 = \sum_{\bar{m}=1}^{\infty}\sum_{\bar{n}=1}^{\infty}\sum_{\bar{l}=1}^{\infty}\left(A_{\bar{m}\bar{n}\bar{l}}\cos\left(\frac{\bar{m}\pi}{a}x\right)\cos\left(\frac{\bar{n}\pi}{b}y\right)Z_{1\bar{l}}\right.$$
$$\left.\exp\left(-t\left(\left(\frac{\bar{m}\pi\sqrt{\alpha_1}}{a}\right)^2+\left(\frac{\bar{n}\pi\sqrt{\alpha_1}}{b}\right)^2+\nu_{\bar{l}}^2\right)\right)\right). \tag{29}$$

From (2) and (3)

$$F_1 = -\theta_{1,s}(x,y,z) \tag{30}$$

and

$$F_2 = -\theta_{2,s}(x,y,z) \tag{31}$$

where $\theta_{1,s}(x,y,z)$ and $\theta_{2,s}(x,y,z)$ are derived in [33]. As

$$\int_0^a \cos\left(\frac{m\pi}{a}x\right)\mathrm{d}x = 0 \text{ and } \int_0^b \cos\left(\frac{n\pi}{b}y\right)\mathrm{d}y = 0$$

$$A_{00\bar{l}} = -\frac{1}{N_{\bar{l}}}\left[\frac{k_1}{\alpha_1}\int_0^{t_1} A_{10}Z_{1\bar{l}}\mathrm{d}z + \frac{k_2}{\alpha_2}\int_{t_1}^{t_1+t_2} A_{20}Z_{2\bar{l}}\mathrm{d}z\right.$$
$$\left.+\frac{k_1}{\alpha_1}\int_0^{t_1} B_{10}zZ_{1\bar{l}}\mathrm{d}z + \frac{k_2}{\alpha_2}\int_{t_1}^{t_1+t_2} B_{20}zZ_{2\bar{l}}\mathrm{d}z\right]. \tag{32}$$

By using the orthogonality relations of the cosine function it can be shown that

$$A_{\bar{m}0\bar{l}} = -\frac{1}{N_{\bar{l}}}\left[\frac{k_1}{\alpha_1}\int_0^{t_1}\left(A_{1\bar{m}}\sinh\left(\frac{\bar{m}\pi}{a}z\right)\right.\right.$$
$$\left.+B_{1\bar{m}}\cosh\left(\frac{\bar{m}\pi}{a}z\right)\right)Z_{1\bar{l}}\mathrm{d}z$$
$$+\frac{k_2}{\alpha_2}\int_{t_1}^{t_1+t_2}\left(A_{2\bar{m}}\cosh\left(\frac{\bar{m}\pi}{a}z\right)\right.$$
$$\left.\left.+B_2\sinh\left(\frac{\bar{m}\pi}{a}z\right)\right)Z_{2\bar{l}}\mathrm{d}z\right]. \tag{33}$$

Similarly

$$A_{0\bar{n}\bar{l}} = -\frac{1}{N_{\bar{l}}}\left[\frac{k_1}{\alpha_1}\int_0^{t_1}\left(A_{1\bar{n}}\cosh\left(\frac{\bar{n}\pi}{b}z\right)\right.\right.$$
$$\left.+B_{1\bar{n}}\sinh\left(\frac{\bar{m}\pi}{b}z\right)\right)Z_{1\bar{l}}\mathrm{d}z$$
$$+\frac{k_2}{\alpha_2}\int_{t_1}^{t_1+t_2}\left(A_{2\bar{n}}\cosh\left(\frac{\bar{n}\pi}{b}z\right)\right.$$
$$\left.\left.+B_{2\bar{n}}\sinh\left(\frac{\bar{n}\pi}{b}z\right)\right)Z_{2\bar{l}}\mathrm{d}z\right] \tag{34}$$

and

$$A_{\bar{m}\bar{n}\bar{l}} = -\frac{1}{N_{\bar{l}}}\left[\frac{k_1}{\alpha_1}\int_0^{t_1}\Big(A_{1\bar{m}\bar{n}}\cosh(\beta_{\bar{m}\bar{n}}z)\right.$$
$$+B_{1\bar{m}\bar{n}}\sinh(\beta_{\bar{m}\bar{n}}z)\Big)Z_{1\bar{l}}\mathrm{d}z$$
$$+\frac{k_2}{\alpha_2}\int_{t_1}^{t_1+t_2}\Big(A_{2\bar{m}\bar{n}}\cosh(\beta_{\bar{m}\bar{n}}z)$$
$$\left.+B_{2\bar{m}\bar{n}}\sinh(\beta_{\bar{m}\bar{n}}z)\Big)Z_{2\bar{l}}\mathrm{d}z\right] \tag{35}$$

where

$$\beta_{\bar{m}\bar{n}} = \sqrt{\left(\frac{\bar{m}\pi}{a}\right)^2+\left(\frac{\bar{n}\pi}{b}\right)^2}$$

and A_{10}, B_{20}, $A_{1\bar{m}}$, $B_{1\bar{m}}$, $A_{2\bar{m}}$, $B_{2\bar{m}}$, $A_{1\bar{n}}$, $B_{1\bar{n}}$, $A_{2\bar{n}}$, $B_{2\bar{n}}$, $A_{1\bar{m}\bar{n}}$, $B_{1\bar{m}\bar{n}}$, $A_{2\bar{m}\bar{n}}$, and $B_{2\bar{m}\bar{n}}$ are the Fourier coefficients in the steady-state solution derived in [33].

C. Putting It Together

Now, the transient thermal modeling of a two-layer structure with a single heat source is formally completed. As the system is linear, for multiple heat sources, the temperature field is simply obtained by the summation of the individual temperature field produced by each heat source considered alone. As a result, the procedure detailed above can be used for transient thermal modeling of an N-layer rectangular structure with any number of rectangular heat sources on its top surface. The generalized expression (for an N-layer structure) of the Fourier coefficients are

$$A_{00\bar{l}} = -\frac{1}{N_{\bar{l}}}\left[\sum_{i=1}^{N}\frac{k_i}{\alpha_i}\int_{z_i}^{z_{i+1}}\Big(A_{i0}+zB_{i0}\Big)Z_{i\bar{l}}\mathrm{d}z\right] \tag{36}$$

$$A_{\bar{m}0\bar{l}} = -\frac{1}{N_{\bar{l}}}\left[\sum_{i=1}^{N}\frac{k_i}{\alpha_i}\int_{z_i}^{z_{i+1}}\left(A_{i\bar{m}}\cosh\left(\frac{\bar{m}\pi}{a}z\right)\right.\right.$$
$$\left.\left.+B_{i\bar{m}}\sinh\left(\frac{\bar{m}\pi}{a}z\right)\right)Z_{i\bar{l}}\mathrm{d}z\right] \tag{37}$$

$$A_{0\bar{n}\bar{l}} = -\frac{1}{N_{\bar{l}}}\left[\sum_{i=1}^{N}\frac{k_i}{\alpha_i}\int_{z_i}^{z_{i+1}}\left(A_{i\bar{n}}\cosh\left(\frac{\bar{n}\pi}{b}z\right)\right.\right.$$
$$\left.\left.+B_{i\bar{n}}\sinh\left(\frac{\bar{n}\pi}{b}z\right)\right)Z_{i\bar{l}}\mathrm{d}z\right] \tag{38}$$

and

$$A_{\bar{m}\bar{n}\bar{l}} = -\frac{1}{N_{\bar{l}}}\left[\sum_{i=1}^{N}\frac{k_i}{\alpha_i}\int_{z_i}^{z_{i+1}}\Big(A_{i\bar{m}\bar{n}}\cosh(\beta_{\bar{m}\bar{n}}z)\right.$$
$$\left.+B_{i\bar{m}\bar{n}}\sinh(\beta_{\bar{m}\bar{n}}z)\Big)Z_{i\bar{l}}\mathrm{d}z\right] \tag{39}$$

where

$$N_{\bar{l}} = \sum_{i=1}^{N}\frac{k_i}{\alpha_i}\int_{z_i}^{z_{i+1}} Z_{i\bar{l}}^2\mathrm{d}z$$

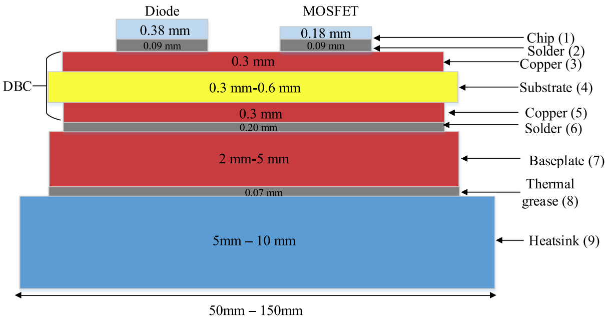

Fig. 4. Cross-sectional view of a typical power module with heatsink.

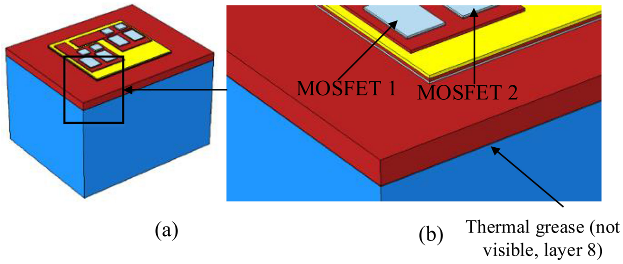

Fig. 5. (a) Three-dimensional view of the PVU. (b) Magnified view of the upper part of the structure.

and

$$Z_{i\bar{l}}(z) = A_{i\bar{l}} \sin\left(\frac{\nu_{\bar{l}} z}{\sqrt{\alpha_i}}\right) + B_{i\bar{l}} \cos\left(\frac{\nu_{\bar{l}} z}{\sqrt{\alpha_i}}\right). \tag{40}$$

It is important to highlight that the eigenvalues and the coefficients of eigenfunctions need only be determined once for a particular problem geometry. Once found, these can be readily used in the calculation of the temperature for any transient heat input.

IV. APPLICATION OF THE THERMAL MODEL OF AN N-LAYER STRUCTURE TO A POWER MODULE

A. Structure of the Power Module

Fig. 4 shows the cross section of a typical power module attached to a heatsink. It is important to emphasize that this is not the representation of the power module considered in this work. As discussed in our previous paper [33], the continuous copper layer, area dissipation, and continuous solder layer (CAC) structure gives good results because the patterning of the copper and the limited extent of the DBC stack does not greatly affect the temperature field, particularly in the important regions around the die. Therefore, this structure is used again in this article to compare with the patterned copper layer, volume dissipation, under the solder layer (PVU) structure which exactly represents the power module. Both structures are described in Figs. 5 and 6. The previous paper contains the details of the module used for experimental verification and so for the brevity this is not repeated here apart from Table I which includes densities and specific heat capacities of the different materials used in the power module.

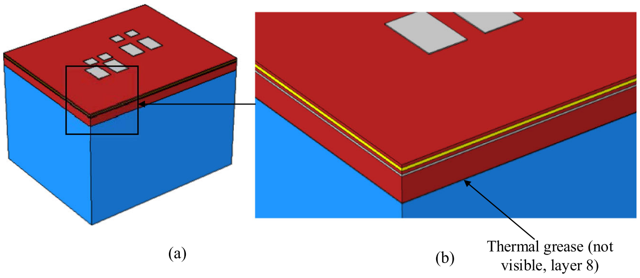

Fig. 6. (a) Three-dimensional view of both the CAU. (b) Magnified view of the upper part of the structure.

TABLE I
MATERIAL PROPERTIES FOR THE SiC POWER MODULE (PART NO. APTMC120AM20CT1NG, COURTESY OF MICROSEMI POWER MODULE PRODUCTS)

Materials	Density (ρ) (kg/m^3)	Specific heat capacity (c) (J/(kgK))	Thermal conductivity (k) (W/(mK))	Thermal diffusivity (α) (cm^2/s)
SiC	3216	690	370	1.67
Si$_3$N$_4$	3100	700	90	0.415
Solder (die attach)	10700	150	30	0.187
Copper	8960	385	390	1.13
Solder (DBC attach)	7400	240	30	0.169
Thermal grease	2500	3000	2.5	0.00330
Aluminium alloy	2700	900	180	0.741

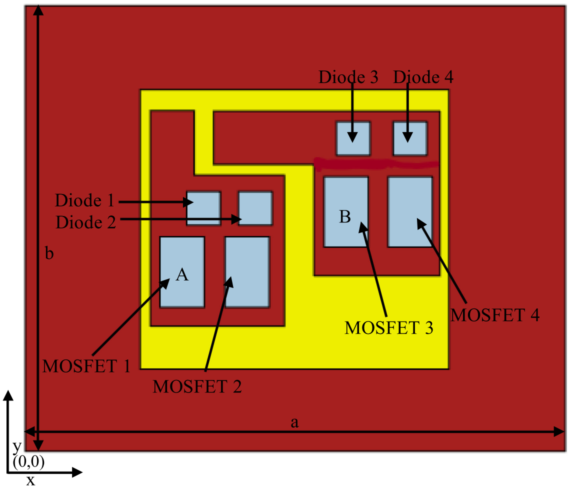

Fig. 7. Top view of the commercial power module used in this work and the position of examination points.

B. Simulation Results and Discussion

For the model and simulation, the heat dissipation (step input) in MOSFETS M1-4 are 63.8, 63.8, 76.9, and 76.9 W, respectively. Figs. 8 and 9 show the comparison of the temperature response for the midpoints of MOSFET M1 and M3 (shown in Fig. 7) predicted by the PVU structure solved in COMSOL Multiphysics and the simplified CAC structure model solved by the TRLNF method. It is important to highlight that *area dissipation* means

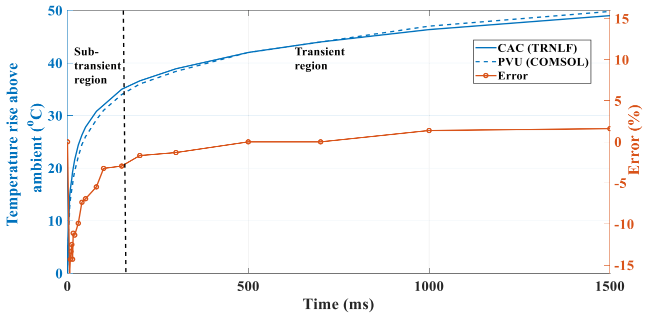

Fig. 8. Comparison between the PVU and the CAC for point A.

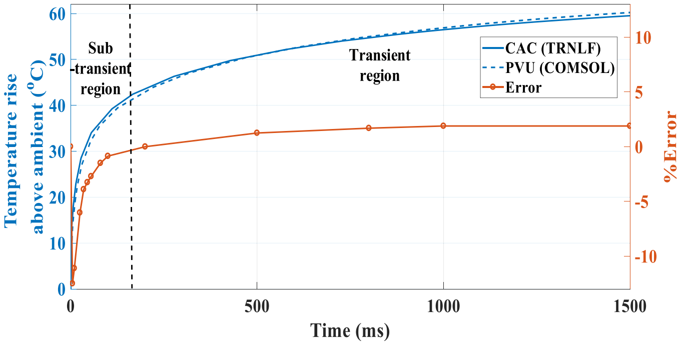

Fig. 9. Comparison between the PVU and the CAC for point B.

there is no die and all the heat enters the corresponding chip area perpendicularly to the surface. *Volume dissipation* means the presence of the die with internal heat generation. For the detailed description of the differences between these models, please refer to [33]. The error at any point in time is defined by the following:

$$\text{error}(t) = \frac{T_{\text{PVU}}(t) - T_{\text{CAC}}(t)}{T_{\text{PVU}}(t) - T_{\text{amb}}} \tag{41}$$

where $T_{\text{PVU}}(t)$ is the simulation temperature for the PVU structure, $T_{\text{M}}(t)$ is the temperature for the CAC structure obtained from model, and T_{amb} is the ambient temperature.

Figs. 8 and 9 can be roughly divided into two regions. The rate of temperature rise in the subtransient region is significantly higher than that in the transient region. The TRLNF model predicts higher temperature than that given by the PVU structure FEM simulation in the subtransient region. This is because, in the CAC model, heat flux is constant on the top surface at all times. In contrast, in the PVU model, the finite thermal diffusivity of the die material is included and therefore it takes a short period for the heat flux at the top of the solder layer to reach a constant value. This is a small effect as the die is physically small and the thermal diffusivity of silicon carbide is relatively high. When the die approaches thermal equilibrium the PVU model gives a slightly higher temperature than that suggested by the CAC model. This is because the temperature measurement is taken on the top of the die in the PVU model, rather than on the top of the solder as in the CAC model.

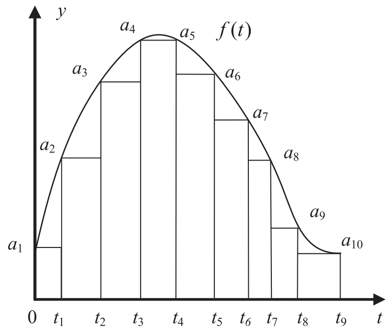

Fig. 10. Arbitrary waveshape with staircase approximation.

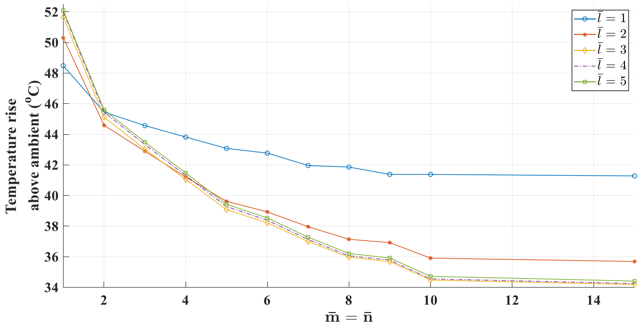

Fig. 11. Convergence of the temperature of the midpoint of MOSFET 3 at $t =$ 60 ms.

In real power electronic applications, the power losses in the semiconductor devices are far more complex than a simple step. Therefore, to apply the TRNLF method in practice it is necessary to determine the temperature-response to an arbitrary load profile. The waveshape in Fig. 10 ($f(t)$) is approximated by a sequence of a rectangular pulses. If θ is the temperature response to the waveshape then using the linearity of the system the following can be written as:

$$\theta = a_1\theta_0 + (a_2 - a_1)\theta_1 + \cdots + (a_N - a_{N-1})\theta_{N-1} - a_N\theta_N \tag{42}$$

where θ_0 is the temperature response to heat pulse $u(t)$, θ_1 is the temperature response to $u(t - t_1)$, θ_2 is the temperature response to $u(t - t_2)$, and so on. If the the waveshape is approximated by more, shorter duration, rectangular pulses, the accuracy of the result will tend to increase.

C. *Convergence of the Transient Thermal Model or TRNLF Method*

The Fourier series representation of the temperature contains an infinite number of terms. In practice, a truncated form of the Fourier series is used, which raises the issue of convergence. The function of the temperature field meets Dirichlet's condition, so it converges at every point of continuity. Fig. 11 shows the comparison of the temperature response for the midpoint of MOSFET M3 for the CAC structure predicted by COMSOL Multiphysics and TRNLF method and the convergence of the latter at $t = 60$ ms. The heat dissipation (step input) in MOSFETs M1-4 are 63.8, 63.8, 76.9 and 76.9 W, respectively. The error at

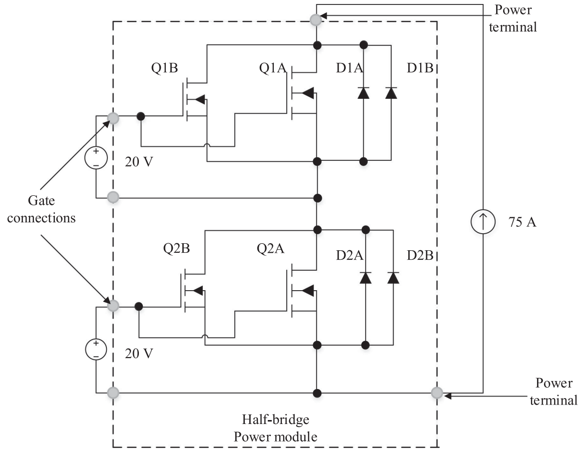

Fig. 12. Schematic diagram of the circuit of the experiment.

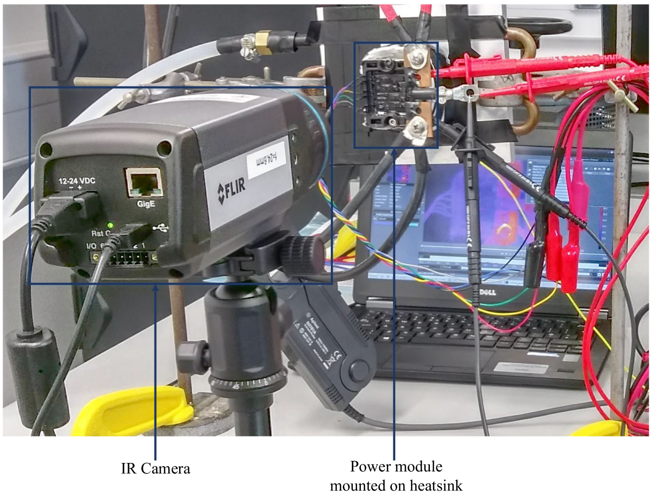

Fig. 13. Experimental setup showing the thermal camera and power module.

$t = 60$ ms is defined by the following:

$$\text{error}(t) = \frac{34.3 - T_{\mathrm{M}}}{34.3 - T_{\mathrm{amb}}} \tag{43}$$

where 34.3 is the simulation temperature (°C), T_{M} is the model temperature, and T_{amb} is the ambient temperature. This figure shows the convergence of temperature for different values of $\bar{l}$ (number of eigenvalues associated with the eigenfunctions in z-direction). It is observed that the effect of $\bar{l}$ on the convergence of the temperature is relatively weak compared to that of $\bar{m}$ or $\bar{n}$ (only a small value of $\bar{l}$ is required to reach the convergence). In $A_{\bar{m}0\bar{l}}$, $A_{0\bar{n}\bar{l}}$, and $A_{\bar{m}\bar{n}\bar{l}}$ [see (37)–(39), respectively], $\bar{m}$ and $\bar{n}$ are present explicitly in the arguments of sine and cosine hyperbolic functions. These functions are unbounded and increase exponentially with the increment of arguments. On the other hand, $\bar{l}$ only affects the sinusoidal terms of the eigenfunctions in z-direction which are bounded. Therefore, the effect of $\bar{m}$ or $\bar{n}$ is more pronounced on the temperature than that of $\bar{l}$. Based on this observation and analysis, it can be concluded that a low value of $\bar{l}$ will typically suffice for the accurate calculation of temperature.

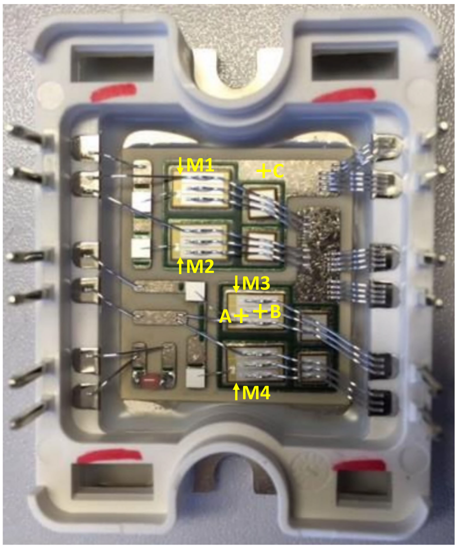

Fig. 14. Location of MOSFET dies M1-4 and points A, B, and C on the power module.

D. Dimensional Nature of the Heat Transfer Problem in the Power Module

An important implication of the TRNLF method is that it provides insight into the dimensional nature of the heat transfer problem, i.e., the extent of heat spreading in different direction. It was observed in the analysis that $\theta_{1,t}$ has four components: M_1, M_2, M_3, and M_4. Only the terms corresponding to z are present in M_1. Terms corresponding to x and z are present in M_2, terms corresponding to y and z are present in M_3 and terms corresponding to x, y and z are present in M_4. Therefore, M_1 represents 1-D heat transfer, M_2 and M_3 represent 2-D heat spreading and M_4 represents 3-D heat spreading. For the example considered in the previous section on convergence, $M_1 = -0.49$ °C, $M_2 = -4.81$ °C, $M_3 = -2.96$ °C, and $M_4 = -10.60$ °C. Therefore, M_4 constitutes a significant portion of the temperature distribution and hence the heat transfer problem is essentially 3-D in nature.

V. EXPERIMENTAL VALIDATION

A. Experimental Setup (See Fig. 13)

An experiment is carried out to validate the TRNLF model and COMSOL Multiphysics solutions using a SiC power module from Microchip Inc. A thermal camera with video capturing facility (FLIR A655sc 25°) is used. A current probe is used to measure the current flowing through the MOSFETs. A digital oscilloscope is used to measure the drain-source voltage of each MOSFET and hence allow the power dissipation of the MOSFETs to be calculated (current is assumed to be split equally between the parallel connected MOSFET dies). At the beginning of the

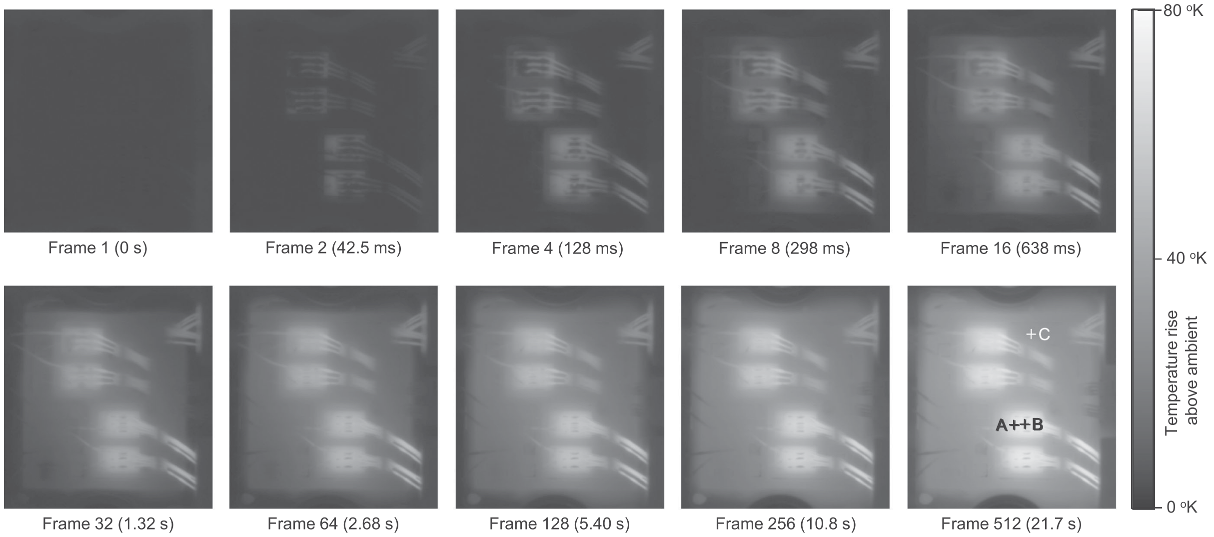
Frame 1 (0 s)
Frame 2 (42.5 ms)
Frame 4 (128 ms)
Frame 8 (298 ms)
Frame 16 (638 ms)
Frame 32 (1.32 s)
Frame 64 (2.68 s)
Frame 128 (5.40 s)
Frame 256 (10.8 s)
Frame 512 (21.7 s)

Fig. 15. Series of frames showing the temperature on the surface of the module.

experiment, the MOSFETs are held on continuously using a constant gate-source voltage of 20 V. The dc power source is turned ON and the resulting transient thermal behavior is recorded by the camera. The mechanical setup is essentially the same as that used in the experiment to validate the steady-state thermal model which is described in [33]. The circuit diagram of the experiment is given in Fig. 12

1) Validity of Assumptions and Boundary Conditions: A conventional power module is encapsulated by plastic and the gap between the top surface (where the dies are situated) and plastic casing is filled by silicon gel [35] for improved electrical insulation. Therefore, the assumptions that the sides and top surface are adiabatic are reasonable. A chiller bath circulates water through a cold plate which is thermally connected to the heatsink. The assumption of perfect thermal contact between different layers was also validated in [33]. The thermal grease layer is modeled as a layer of uniform thickness. A requirement for the experiment is to create an isothermal surface as a boundary condition because the detailed modeling of the liquid-cooled heatsink or the thermal coupling between the power module and the heatsink is not a part of the TRNLF method; a relatively thick heat-spreader made of aluminum alloy is used to create this condition. The position of the isothermal plane situated within the heat spreader is exactly the same as that in our previous work [33].

B. Conditioning of the Module

In order to allow accurate thermal imaging, the module used in this work was provided by the manufacturer without any silicon gel (see Fig. 14). The surface of the module is replete with shiny copper traces, semiconductor devices, and wirebonds with an emissivity much lower than 1, which would hinder the IR camera from capturing accurate data. Therefore, black paint is sprayed a number of times over the top surface of the power module in order to raise the emissivity to close to 1. The value of emissivity setting used in this work is 0.98.

C. Experimental Results and Discussion

The MOSFET dies are denoted by M1, M2, M3, and M4, respectively. The midpoint (corresponding to point B in Fig. 14) of MOSFET 3 is obstructed by a bondwire and so the temperature measured at this point does not accurately effect the real temperature of the die. Hence, a point unobstructed by the bondwire (corresponding to point A) yet close to the midpoint is used instead. A series of snapshots taken from the video data of the power module operating during the thermal transient is presented in Fig. 15. It can be seen that the heat generated by the MOSFET dies diffuses throughout the module over a period of about 3 s.

The detector of the camera used in this experiment is described by the manufacturer as having a time constant of approximately 10 ms. It is assumed that this camera works as a first-order low-pass filter with unity gain according to

$$H(s) = \frac{1}{1 + s\tau_c} \tag{44}$$

where $\tau_c = 10$ ms is the time constant of the filter. After the data from the model/simulation are passed through this filter, a close match with the experimental data is achieved, as shown in Figs. 16 and 17. The error between the filtered data and experimental data is given by

$$\text{error}(t) = \frac{T_{\text{exp}}(t) - T_{\text{filter}}(t)}{T_{\text{exp}}(t) - T_{\text{amb}}} \tag{45}$$

where T_{exp} is experimental data T_{filter} is filtered data. The maximum error in the subtransient and transient regions is approximately -5% and 3%, respectively.

1) Comparison Between the Experiment and Simulation/Model for Another Point on the Module: A better match between the experiment and simulation/model can be expected at points where the temperature change is relatively slow because the limited frequency response of the thermal camera will have less effect. Such a point is C which is situated on the first copper layer of the DBC substrate. A good match

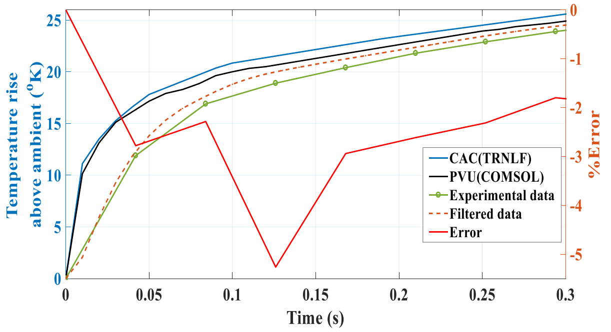

Fig. 16. Comparison between experimental, simulation, and low-pass filtered simulation for point A in the subtransient region.

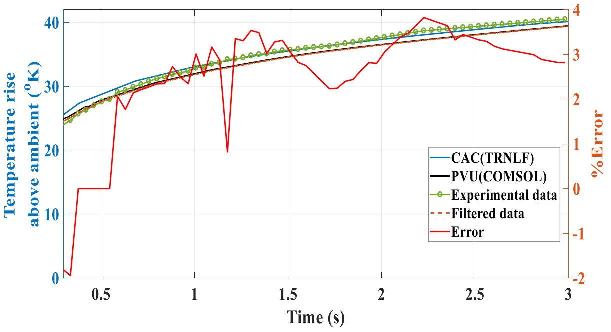

Fig. 17. Comparison between experimental, simulation, and low-pass filtered simulation for point A in the transient region.

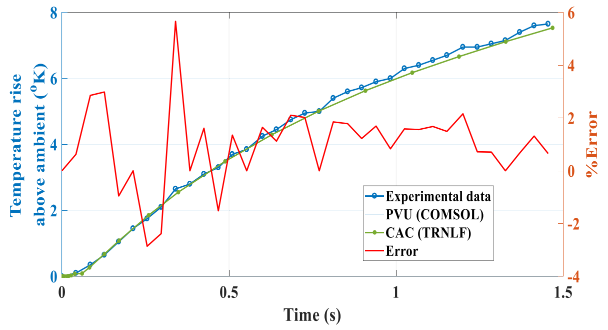

Fig. 18. Comparison between the experiment and simulation for point C.

between the experiment and simulation/model is observed for this point (see Fig. 18) without the application of the low-pass filter.

2) Comparison of Computational Time: The total computational effort required by the TRNLF method can be separated into three parts—time to extract eigenvalues, time to calculate the coefficients of the eigenfunctions, and time to calculate the temperature response. For the examples used in this article, using a relatively unoptimized MATLAB script running on a standard laptop (Intel Core i5 7200 U, 8-GB RAM), the time taken to extract 25 eigenvalues is approximately 3.5 min, time taken to calculate the coefficients is approximately 40 s, and time taken to calculate the temperature of a single point in space at a particular instant in time is 2–3 s. Therefore, the total time taken to compute the temperature response of a single point is dominated by the calculation of eigenvalues and the coefficients of eigenfunctions. However, the eigenvalues and the coefficients of eigenfunctions only need to be evaluated once for a particular geometry and material combination (see Fig. 2). Once this is done, the temperature response to a step input (and by implication, an arbitrary waveshape) can be calculated quickly. Importantly, the determination of eigenvalues and coefficients only depend on thickness and material properties of each layer, not on the length and width or the position of the chip. As a result, the TRNLF method may be useful for thermal optimization in applications where the thickness and material of each layer is fixed (for example where chip position is being optimised independent of material selection). In contrast, a simulation in COMSOL Multiphysics cannot directly calculate the temperature response at a particular space/time point; an FEM system must solve the whole system for previous instants. As a comparison, on the same machine, COMSOL Multiphysics takes approximately 10–12 min to calculate the temperature field at $t = 3$ s using the default settings.

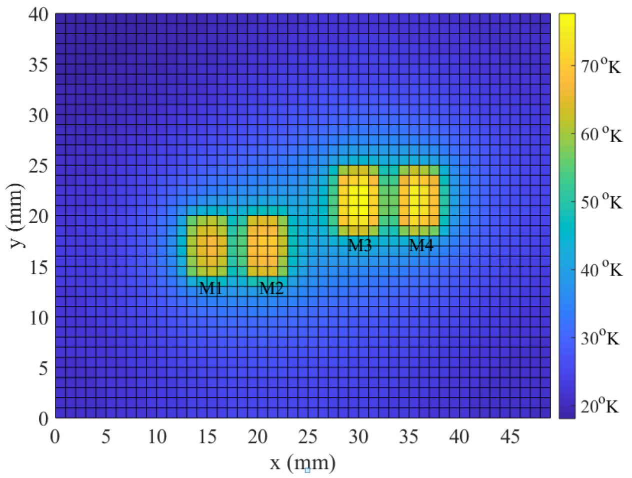

Fig. 19. Distribution of temperature rise over the surface of MOSFET 3 obtained from the TRNLF method for $t = 10.8$ s.

The time taken to calculate the temperature response increases with the number of points under consideration. Hence, the TRNLF method may not offer much computational advantage if the number of points for the temperature calculation is large. Fig. 19 shows the temperature distribution on the surface of MOSFET 3 at $t = 10.8$ s (corresponding to frame 256 in Fig. 15) obtained by TRNLF method where 2050 points (a mesh size of 1 mm) are considered. The total time taken for the whole calculation is approximately 15 min (4 min for the calculation of eigenvalues and coefficients, plus 11 min for 2050 points).

VI. CONCLUSION

A semianalytical method of transient thermal modeling (the TRNLF method) is presented in this article. This method is validated against FEM simulation and experiment. An excellent match is observed between the model, simulation, and experiment, once the time constant of the thermal camera used in this experiment is taken into account. Although 3-D analytical/semianalytical methods have been investigated previously, Fourier-based 3-D transient models for an arbitrary N-layer rectangular structure have not. A major strength of this method is the relatively straightforward and general expression of Fourier coefficients compared to those of [28]. Moreover, the method does not require a large matrix inversion which is necessary in [22] and [23] or other mesh-based solutions (the steady-state solution derived in [33] does not require any matrix operation). Like the RNLF method presented in our previous paper, the TRNLF method is smooth with dimensional changes and computationally efficient when evaluating the temperatures of a few points. Although the focus of this article has been on power modules, the TRNLF method may find other applications in layered structures, assuming that suitable simplifications can be made in these cases.

APPENDIX A
THERMAL SPREADING RESISTANCE

The thermal spreading resistance may be computed using the mean temperature-rise of the heat source. From [33]

$$\begin{aligned}\theta_{1,s}(x,y,z) &= A_{10} + B_{10}z + \sum_{\bar m=1}^{\infty}\cos\left(\frac{\bar m\pi}{a}x\right)\\ &\times\left[A_{1\bar m}\cosh\left(\frac{\bar n\pi}{a}z\right) + B_{1\bar m}\sinh\left(\frac{\bar m\pi}{a}z\right)\right]\\ &+\sum_{\bar n=1}^{\infty}\cos\left(\frac{\bar n\pi}{b}y\right)\left[A_{1\bar n}\cosh\left(\frac{\bar n\pi}{b}z\right)+B_{1\bar n}\sinh\left(\frac{\bar n\pi}{b}z\right)\right]\\ &+\sum_{\bar m=1}^{\infty}\sum_{\bar n=1}^{\infty}\cos\left(\frac{\bar m\pi}{a}x\right)\cos\left(\frac{\bar n\pi}{b}y\right)\Big[A_{1\bar m\bar n}\cosh(\beta_{\bar m\bar n}z)\\ &+B_{1\bar m\bar n}\sinh(\beta_{\bar m\bar n}z)\Big].\end{aligned}\tag{46}$$

The average temperature-rise of the heat source can be obtained by integrating (46) over the heat source area. Executing the necessary mathematical operations leads to the following expression for the average temperature-rise:

$$\begin{aligned}\bar\theta_1(x,y,z) &= A_{10} + 2\sum_{\bar m=1}^{\infty}A_{1\bar m}\frac{\cos(\lambda_{\bar m}X_c)\sin(\frac{1}{2}\lambda_{\bar m}c)}{\lambda_{\bar m}c}\\ &+2\sum_{\bar n=1}^{\infty}A_{1\bar n}\frac{\cos(\delta_{\bar n}Y_c)\sin(\frac{1}{2}\delta_{\bar n}d)}{\delta_{\bar n}d} + 4\sum_{\bar m=1}^{\infty}\sum_{\bar n=1}^{\infty}A_{1\bar m\bar n}\\ &\frac{\cos(\delta_{\bar n}Y_c)\sin(\frac{1}{2}\delta_{\bar n}d)\cos(\lambda_{\bar m}X_c)\sin(\frac{1}{2}\lambda_{\bar m}c)}{\delta_{\bar n}\lambda_{\bar m}dc}\end{aligned}\tag{47}$$

where

$$\lambda_{\bar m} = \frac{\bar m\pi}{a}, \delta_{\bar n} = \frac{\bar n\pi}{b}.$$

It is important to highlight that (47) is similar to the expression of average temperature-rise or thermal resistance derived in [36].

TABLE II
ONE-DIMENSIONAL AND SPREADING THERMAL RESISTANCES OF MOSFETS FOR THE SiC POWER MODULE

MOSFET	X_c (mm)	Y_c (mm)	R_{sp} (K/W)
1	14.41	16.43	0.4074
2	20.34	16.43	0.4074
3	29.38	21.03	0.4076
4	35.65	21.03	0.4076
example	45.00	37.00	0.4524

Now, thermal spreading resistance, R_{sp} is calculated as

$$R_T = \frac{\bar\theta_{1,s}}{Q} = R_{1D} + R_{sp}\tag{48}$$

where R_{1D} is the 1-D thermal resistance. By inspection, it can be said that series terms in (47) are the thermal spreading resistance and $R_{1D} = A_{10}$ is the 1-D thermal resistance which is equal to 0.01075 K/W for all MOSFETs. The spreading thermal resistances associated with each MOSFET are given in Table II.

The spreading thermal resistances of MOSFETs 1–4 are very similar because they are all placed near the centre of the module and so share very similar thermal paths to ambient. An example MOSFET placed near the corner of the module exhibits a significantly larger spreading thermal resistance. Note that MOSFETs 3 and 4 exhibit higher temperatures because they dissipate more power compared to MOSFETs 1 and 2, not because they have a higher spreading resistance.

ACKNOWLEDGMENT

The authors would like to thank S. Bontemps at Microchip Inc. for supplying the sample SiC MOSFET power module and corresponding dimensions and material properties used in the article, and D. Howey of the University of Oxford for use of the thermal camera.

REFERENCES

[1] M. Musallam and C. M. Johnson, “Real-time compact thermal models for health management of power electronics,” *IEEE Trans. Power Electron.*, vol. 25, no. 6, pp. 1416–1425, Jun. 2010.

[2] P. Hagler, P. Henson, and R. W. Johnson, “Packaging technology for electronic applications in harsh high-temperature environments,” *IEEE Trans. Ind. Electron.*, vol. 58, no. 7, pp. 2673–2682, Jul. 2011.

[3] S. Yang, A. Bryant, P. Mawby, D. Xiang, L. Ran, and P. Tavner, “An industry-based survey of reliability in power electronic converters,” *IEEE Trans. Ind. Appl.*, vol. 47, no. 3, pp. 1441–1451, May 2011.

[4] R. John, O. Vermesan, and R. Bayerer, “High temperature power electronics IGBT modules for electrical and hybrid vehicles,” in *Proc. IMAPS, High Temp. Electron. Netw.*, 2009, vol. 1, pp. 199–204.

[5] R. Pittini, S. D’Arco, M. Hernes, and A. Petterteig, “Thermal stress analysis of IGBT modules in VSCS for PMSG in large offshore wind energy conversion systems,” in *Proc. IEEE 14th Eur. Conf. Power Electron. Appl.*, 2011, pp. 1–10.

[6] H. Chen, B. Ji, V. Pickert, and W. Cao, “Real-time temperature estimation for power MOSFETs considering thermal aging effects,” *IEEE Trans. Device Mater. Rel.*, vol. 14, no. 1, pp. 220–228, Mar. 2014.

[7] Y. Avenas, L. Dupont, and Z. Khatir, “Temperature measurement of power semiconductor devices by thermo-sensitive electrical parameters—A review,” *IEEE Trans. Power Electron.*, vol. 27, no. 6, pp. 3081–3092, Jun. 2012.

[8] N. Baker, M. Liserre, L. Dupont, and Y. Avenas, "Improved reliability of power modules: A review of online junction temperature measurement methods," *IEEE Ind. Electron. Mag.*, vol. 8, no. 3, pp. 17–27, Sep. 2014.

[9] H. Huang and P. Mawby, "A lifetime estimation technique for voltage source inverters," *IEEE Trans. Power Electron.*, vol. 28, no. 8, pp. 4113–4119, Aug. 2013.

[10] M. Musallam, C. M. Johnson, C. Yin, H. Lu, and C. Bailey, "In-service life consumption estimation in power modules," in *Proc. IEEE 13th Int. Power Electron. Motion Control Conf.*, 2008, pp. 76–83.

[11] N. Patil, J. Celaya, D. Das, K. Goebel, and M. Pecht, "Precursor parameter identification for insulated gate bipolar transistor (IGBT) prognostics," *IEEE Trans. Rel.*, vol. 58, no. 2, pp. 271–276, Jun. 2009.

[12] N. Patil, D. Das, and M. Pecht, "A prognostic approach for non-punch through and field stop IGBTs," *Microelectron. Rel.*, vol. 52, no. 3, pp. 482–488, 2012.

[13] R. Ovando, F. Ramírez, C. Hernandez, and M. Arjona, "A 2-D finite element thermal model of a three-phase-inverter heat sink," in *Proc. IEEE Electron., Robot. Automot. Mech. Conf.*, 2010, pp. 696–701.

[14] J. Reichl, J. M. Ortiz-Rodriguez, A. Hefner, and J.-S. Lai, "3-D thermal component model for electrothermal analysis of multichip power modules with experimental validation," *IEEE Trans. Power Electron.*, vol. 30, no. 6, pp. 3300–3308, Jun. 2015.

[15] M. Ouhab, Z. Khatir, A. Ibrahim, J.-P. Ousten, R. Mitova, and M.-X. Wang, "New analytical model for real-time junction temperature estimation of multichip power module used in a motor drive," *IEEE Trans. Power Electron.*, vol. 33, no. 6, pp. 5292–5301, Jun. 2018.

[16] S. Carubelli and Z. Khatir, "Experimental validation of a thermal modelling method dedicated to multichip power modules in operating conditions," *Microelectron. J.*, vol. 34, no. 12, pp. 1143–1151, 2003.

[17] M. Ciappa, W. Fichtner, T. Kojima, Y. Yamada, and Y. Nishibe, "Extraction of accurate thermal compact models for fast electro-thermal simulation of IGBT modules in hybrid electric vehicles," *Microelectron. Rel.*, vol. 45, nos. 9/11, pp. 1694–1699, 2005.

[18] Z. Zhou, P. Holland, and P. Igic, "Compact thermal model of a three-phase IGBT inverter power module," in *Proc. IEEE 26th Int. Conf. Microelectron.*, 2008, pp. 167–170.

[19] T. Azoui, P. Tounsi, G. Pasquet, P. Dupuy, and J. Dorkel, "Dynamic compact thermal model for electrothermal modeling and design optimization of automotive power devices," in *Proc. IEEE 12th Intl. Conf. Thermal, Mech. Multi-Phys. Simul. Exp. Microelectron. Microsyst.*, 2011, pp. 1–6.

[20] A. Raciti, D. Cristaldi, G. Greco, G. Vinci, and G. Bazzano, "Electrothermal PSpice modeling and simulation of power modules," *IEEE Trans. Ind. Electron.*, vol. 62, no. 10, pp. 6260–6271, Oct. 2015.

[21] M. Musallam and C. M. Johnson, "Monitoring through-life thermal path degradation using real time thermal models," in *Proc. IEEE Power Electron. Specialists Conf.*, 2008, pp. 738–743.

[22] W. Huang, S. Ghosh, S. Velusamy, K. Sankaranarayanan, K. Skadron, and M. R. Stan, "HotSpot: A compact thermal modeling methodology for early-stage vlsi design," *IEEE Trans. Very Large Scale Integration Syst.*, vol. 14, no. 5, pp. 501–513, May 2006.

[23] A. Sridhar, A. Vincenzi, D. Atienza, and T. Brunschwiler, "3D-ICE: A compact thermal model for early-stage design of liquid-cooled ICs," *IEEE Trans. Comput.*, vol. 63, no. 10, pp. 2576–2589, Oct. 2014.

[24] H. Salt, "Transient conduction in a two-dimensional composite slab—I. Theoretical development of temperature modes," *Int. J. Heat Mass Transfer*, vol. 26, no. 11, pp. 1611–1616, 1983.

[25] M. Mikhailov and M. Özişik, "Transient conduction in a three-dimensional composite slab," *Int. J. Heat Mass Transfer*, vol. 29, no. 2, pp. 340–342, 1986.

[26] C. Aviles-Ramos, A. Haji-Sheikh, and J. Beck, "Exact solution of heat conduction in composite materials and application to inverse problems," *J. Heat Transfer*, vol. 120, no. 3, pp. 592–599, 1998.

[27] L. Yan, A. Haji-Sheikh, and J. Beck, "Thermal characteristics of two-layered bodies with embedded thin-film heat source," *J. Electron. Packag.*, vol. 115, no. 3, pp. 276–283, 1993.

[28] V. Kadambi and N. Abuaf, "An analysis of the thermal response of power chip packages," *IEEE Trans. Electron. Devices*, vol. 32, no. 6, pp. 1024–1033, Jun. 1985.

[29] W. Batty, C. E. Christoffersen, A. J. Panks, S. David, C. M. Snowden, and M. B. Steer, "Electrothermal cad of power devices and circuits with fully physical time-dependent compact thermal modeling of complex nonlinear 3-D systems," *IEEE Trans. Compon. Packag. Technol.*, vol. 24, no. 4, pp. 566–590, Dec. 2001.

[30] K. Wang and Z. Pan, "An analytical model for steady-state and transient temperature fields in 3-d integrated circuits," *IEEE Trans. Compon., Packag. Manuf. Technol.*, vol. 6, no. 7, pp. 1026–1039, Jul. 2016.

[31] A. Csendes, V. Szekely, and M. Rencz, "An efficient thermal simulation tool for ICS, microsystem elements and MCMS: The μs-thermanal," *Microelectron. J.*, vol. 29, nos. 4-5, pp. 241–255, 1998.

[32] J.-M. Dorkel, P. Tounsi, and P. Leturcq, "Three-dimensional thermal modeling based on the two-port network theory for hybrid or monolithic integrated power circuits," *IEEE Trans. Compon., Packag., Manuf. Technol.: Part A*, vol. 19, no. 4, pp. 501–507, Dec. 1996.

[33] K. R. Choudhury and D. J. Rogers, "Steady-state thermal modeling of a power module: An n-layer fourier approach," *IEEE Trans. Power Electron.*, vol. 34, no. 2, pp. 1500–1508, Feb. 2019.

[34] M. N. Ozisik, *Heat Conduction*, 1st ed. New York, NY, USA: Wiley, 1980.

[35] M. A. Eleffendi, "In-service estimation of state of health of power modules," Ph.D. dissertation, Univ. Nottingham, Nottingham, U.K., 2015.

[36] Y. Muzychka, J. Culham, and M. Yovanovich, "Thermal spreading resistance of eccentric heat sources on rectangular flux channels," *J. Electron. Packag.*, vol. 125, no. 2, pp. 178–185, 2003.